Published in *Journal of Physics and Chemistry of Solids*, 67 (2006) 2136

Simulations of Dense Atomic Hydrogen in the Wigner Crystal Phase

Burkhard Militzer

Geophysical Laboratory, Carnegie Institution of Washington, 5251 Broad Branch Road, N.W., Washington, DC 20015

Rebekah L. Graham

College of Creative Studies, University of California, Santa Barbara, CA 93106

Abstract

Path integral Monte Carlo simulations are applied to study dense atomic hydrogen in the regime where the protons form a Wigner crystal. The interaction of the protons with the degenerate electron gas is modeled by Thomas-Fermi screening, which leads to a Yukawa potential for the proton-proton interaction. A numerical technique for the derivation of the corresponding action of the paths is described. For one density of $r_s = 200$ (ρ =2,100 g cm^{-3} for hydrogen), the melting properties are studied using the Lindemann ratio, the structure factor, and free energy calculations. Anharmonic effects in the crystal vibrations are analyzed.

Key words:
Path integral Monte Carlo, hydrogen melting, Wigner crystal, pair action
PACS:

1 Introduction

Recent advances in high pressure experiments and computer simulation techniques have led to substantial progress in our understanding of the melting properties of solid hydrogen at high pressure. Using diamond anvil cell experiments, E. Gregoryanz *et al.* [1] extended the experimental determination of the melting line from 15 GPa [2] to 40 GPa. Bonev *et al.* [4] combined the two-phase melting technique with *ab initio* simulations [3] and predicted that there is a maximum in the melting temperature around 80 GPa. At these pressures, hydrogen is still in molecular form. The question of interest is whether the melting temperature keeps decreasing as the pressure is increased further, or if another phase appears and the melting temperature again increases.

From theoretical arguments, we know that atomic hydrogen eventually transforms into a Wigner crystal where the protons form a body centered cubic (b.c.c.) lattice. The focus of this work is to characterize the Wigner crystal regime more accurately and to determine the quantum effects on its melting line. We begin our study with the regime where Jones and Ceperley [5] predicted a maximum on the melting curve of the Wigner crystal, and further focus on one density of $r_s = 200$. The corresponding pressure in hydrogen reaches many peta pascals, which is eight orders of magnitude higher than the giga pascal pressures common in the molecular phase.

In this article, we study the Wigner crystal of protons using path integral Monte Carlo (PIMC). This technique allows us to characterize the quantum effects of the protons. The anharmonic effects in the lattice vibrations are also included accurately. At much higher temperature and lower density, one can describe the electrons from first principles [6]. For this work, we instead approximate the electron-proton interaction using Thomas-Fermi theory. This leads to an effective Yukawa potential for the proton-proton interaction,

$$V_Y(r) = \frac{\mathbf{e}^2}{r} e^{-r/D_s} \ , \tag{1}$$

where the screening length D_s is given by [7],

$$D_s = \left(\frac{\pi}{12}\right)^{1/3} \left(\frac{r_s}{a_0}\right)^{1/2} a_0 \ , \tag{2}$$

and r_s is the Wigner-Seitz radius, $\frac{4}{3}\pi r_s^3 = V/N$. Throughout this work, we will use units of *nuclear* Bohr radii, $a_0 = 4\pi\epsilon_0\hbar^2/m_p e^2 = 2.9{\times}10^{-14}$ m, and *nuclear* Hartrees, Ha $= e^2/(4\pi\epsilon_0 a_0) = 8.0{\times}10^{-15}$ J $= 5.8 \times 10^8$ K k_b, which are a factor by $m_p/m_e = 1836$ less, or greater respectively, than the usual atomic units.

Jones and Ceperley [5] used PIMC to study quantum melting in Coulomb systems where the electrons were assumed to form a rigid background. We extend their work by introducing the Yukawa potential, in order to understand how the electronic screening affects the stability of the Wigner crystal. Ceperley and coworkers have used this potential to study the ground state of interacting fermions [8] and bosons [9] as an model system representing neutron matter. For those applications the screening length is much shorter and the Ewald break-up of the potential discussed in the following section can be avoided. Mon *et al.* [10] also used effective pair potentials derived from linear response theory to study the solid and liquid groundstate energies of dense hydrogen. There it was argued that the proton pair potential can be approximated well by a Yukawa potential for densities higher than $r_s \leq 2500$.

2 Path integral Monte Carlo

The thermodynamic properties of a many-body quantum system at finite temperature can be computed by averaging over the density matrix, $\hat{\rho} = e^{-\beta \hat{H}}, \beta = 1/k_{\rm b}T$. The path integral formalism [11] is based on the identity,

$$\hat{\rho} \equiv e^{-\beta \hat{H}} = \left[e^{-\frac{\beta}{M} \hat{H}} \right]^M \ , \tag{3}$$

where M is a positive integer. Insertion of complete sets of states between the M factors leads to the usual imaginary time path integral formulation, written here in real space,

$$\rho(\mathbf{R}, \mathbf{R}'; \beta) = \int \ldots \int d\mathbf{R}_1 \ldots d\mathbf{R}_{M-1} \, \rho(\mathbf{R}, \mathbf{R}_1; \tau) \ldots \rho(\mathbf{R}_{M-1}, \mathbf{R}'; \tau) \ , \tag{4}$$

where $\tau = \beta/M$ is the time step, and $\mathbf{R}$ is a collective coordinate including all particles, $\mathbf{R} = \{\mathbf{r}_1, \ldots, \mathbf{r}_N\}$. Each of the M steps in the path now has a high temperature density matrix $\rho(\mathbf{R}_k, \mathbf{R}_{k+1}; \tau)$ associated with it. The integrals are evaluated by Monte Carlo methods. For the densities under consideration, we can neglect exchange effects of the protons and represent them by distinguishable particles. Given these constraints, PIMC is an exact technique and free of uncontrolled approximations (assuming the Yukawa potential is valid). This technique includes the correct phonon excitations in the presence of anharmonic effects, which we will discuss later.

2.1 Action for an Isolated Pair of Particles

The action plays a central role in PIMC, since it determines the weights of paths. We will describe a novel approach for its derivation, which we found to be more accurate for Yukawa systems than previous techniques. First we discuss the action for an isolated pair of particles, and then we introduce periodic boundary conditions commonly used in many-body simulations.

Typically, one approximates the high-temperature many-body density matrix, $\rho(\mathbf{R}, \mathbf{R}'; \tau)$, as a product of exact pair density matrices which can be motivated using the Feynman-Kac (FK) formula,

$$\frac{\rho(\mathbf{R}, \mathbf{R}'; \tau)}{\rho_0(\mathbf{R}, \mathbf{R}'; \tau)} = \left\langle e^{-\int_0^\tau dt \sum_{i<j} V_Y(\mathbf{r}_{ij})} \right\rangle_{\mathbf{R} \to \mathbf{R}'} = \left\langle \prod_{i<j} e^{-\int_0^\tau dt V_Y(\mathbf{r}_{ij})} \right\rangle_{\mathbf{R} \to \mathbf{R}'} \tag{5}$$

$$\approx \prod_{i<j} \left\langle e^{-\int_0^\tau dt V_Y(\mathbf{r}_{ij})} \right\rangle_{\mathbf{r}_{\rm ij} \to \mathbf{r}'_{\rm ij}} \equiv e^{-\sum_{i<j} U_Y(\mathbf{r}_{ij}, \mathbf{r}'_{ij}; \tau)}, \tag{6}$$

where $\rho_0(\mathbf{R}, \mathbf{R}'; \tau)$ is the free particle density matrix. $U_Y(\mathbf{r}_{ij}, \mathbf{r}'_{ij}; \tau)$ is the pair action corresponding to all paths separated by $\mathbf{r}_{ij}$ at imaginary time $t = 0$ and by $\mathbf{r}'_{ij}$ at $t = \tau$. An approximation is introduced when one makes the assumption that the different pair interactions can be averaged by independent Brownian random walks, denoted by brackets $\langle \ldots \rangle$. The pair action approximation is exact for the two particle problem. However, higher-order correlations are left out, which must be recovered in the many-body PIMC simulations using a sufficiently small time step τ.

The pair action, U_Y, can be computed by three different methods. 1) For certain potentials where the eigenstates are known in analytical form, e.g. for the Coulomb potential, the action can be derived from the sum of eigenstates [12]. However to our knowledge, for the Yukawa potential they are not known analytically. 2) In the matrix squaring technique [13], one represents the density matrix on a grid and successively lowers the temperature by performing a one-step path integration. This method can be applied to arbitrary potentials. 3) For the Yukawa potential, we found it advantageous to use the FK formula to derive the pair action. Computationally, it is a bit more expansive than matrix squaring but it does not introduce grid errors that we found difficult to control in case of the Yukawa potential. The FK approach is also applicable to arbitrary potentials unless they exhibit an attractive singularity, which is discussed further in [14].

In the FK approach, one derives the action $U_Y(\mathbf{r}, \mathbf{r}'; \beta)$ stochastically by generating an ensemble of random paths according to the free particle action $U_0(\mathbf{r}, \mathbf{r}'; \beta)$ that begin at $\mathbf{r}$ and terminate at $\mathbf{r}'$,

$$e^{-(U_Y - U_0)} = \left\langle e^{-\tau/2 \sum_{i=1}^{M} [V_Y(\mathbf{r}_{i-1}) + V_Y(\mathbf{r}_i)]} \right\rangle_{U_0(\mathbf{r}, \mathbf{r}'; \beta)} . \tag{7}$$

The free-particle paths can be generated by a bisection algorithm [15]. We found that $M = \beta/\tau = 32$ time steps was sufficient for the Yukawa potential.

To determine the kinetic energy in simulations, one also needs the derivative of the action with respect to β [15], which can be evaluated from the same set of paths like Eq. 7,

$$\frac{\partial}{\partial \beta}(U_Y - U_0) = \left\langle e^{-\sum_i \tau V_Y(\mathbf{r}_i)} \frac{1}{M} \sum_{i=1}^{M} \left[V_Y(\mathbf{r}_i) + \frac{1}{2}(\mathbf{r}_i - \mathbf{r}_i^{\mathrm{Cl}}) \cdot \nabla V_Y(\mathbf{r}_i) \right] \right\rangle_{U_0(\mathbf{r}, \mathbf{r}'; \beta)} ,$$

where $\mathbf{r}_i^{\mathrm{Cl}}$ represents the classical path between the two end points.

The FK formula yields the action for only one specific pair of $\mathbf{r}$ to $\mathbf{r}'$. For the diagonal action, $\mathbf{r} = \mathbf{r}'$, we map out a whole grid of points beginning from

a small value near the origin to large values (several times the thermal de Broglie wavelength given by $\sqrt{2\pi\hbar^2\beta/m}$). Typically, we use a logarithmic grid with about 500 points. For large r, the action approaches the classical limit given by the primitive approximation,

$$U_Y(\mathbf{r},\mathbf{r}';\beta) \approx \frac{\beta}{2}\left[V_Y(\mathbf{r}) + V_Y(\mathbf{r}')\right] \ , \tag{8}$$

which is shown in Fig. 1.

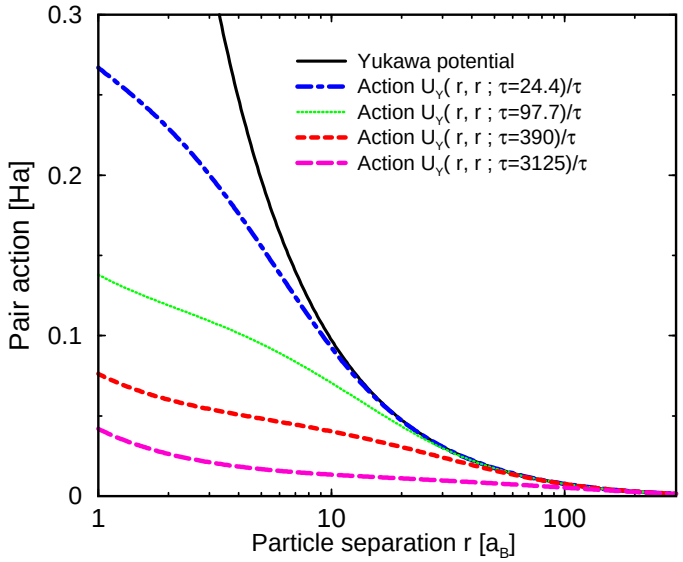

Fig. 1. The pair action $U_Y(r, r' = r; \tau)$, scaled by $1/\tau$, is compared with the corresponding Yukawa potential as a function path separation, r. The Yukawa screening length of $D_s = 387$ represents the electronic screening of the proton interaction in hydrogen at a density of $r_s = 200$. The action converges to the primitive approximation, Eq. 8, for large r and small τ. At small r, quantum fluctuations remove the singularity present in the Yukawa potential and lead to a linear dependence on r, which is known as the cusp condition.

Statistical uncertainties in the resulting action are intrinsic to the FK approach. We found that 10^6 paths yield sufficiently small error bars. However, any noise in tabulated action values is impractical for the subsequent interpolation in PIMC simulations. To eliminate this problem, we use the same random paths for all grid points in the table. This does not remove the uncertainty but prevents noise in the tables.

Including off-diagonal density matrix elements in PIMC simulations allows one to use larger time steps, which makes the simulation more efficient. However, the off-diagonal terms are more difficult to obtain with the FK approach, which is one of the limitations of the approach. Here, we only consider the

leading term in an expansion of the action [15],

$$U_Y(\mathbf{r},\mathbf{r}';\beta) \approx U_Y(q,q;\beta) + s^2\,\xi(q;\beta) \;+\; \ldots, \tag{9}$$

where $q = \frac{1}{2}(|\mathbf{r}| + |\mathbf{r}'|)$, and $s = |\mathbf{r} - \mathbf{r}'|$. It turns out that it is more efficient to derive ξ from finite differences in s rather than evaluating an analytical expression. Having completed our derivation for the action of an isolated pair of particles, we now consider a system with periodic boundary conditions.

2.2 Pair Action in Periodic Boundary Conditions

For the density under consideration, $r_s = 200$, and the corresponding screening length for hydrogen ($D_s = 387.667$), classical simulations [16] at finite temperature and groundstate quantum calculations [8] predict that b.c.c. is the groundstate crystal structure. In our PIMC simulations, we use $N = 2 * 5^3 = 250$ particles, which are initially placed on the sites of the b.c.c. lattice. Since the screening length is comparable in magnitude to the length of the simulation cell, $L = 1218.59$, long-range effects from periodic image particles are far from negligible, and significant care must be taken to derive results in the thermodynamic limit. In this section we describe how long range interactions can be treated efficiently in PIMC simulations with periodic boundary conditions.

The consideration of periodic image charges removes the most severe finite size dependence. We expect the residual finite size error to be fairly small since we used more particles than in previous Coulomb simulations [17], and the screening is expected to reduce finite size effects. Based on the finite size scaling by Jones and Ceperley [17], we estimate the uncertainty of our melting temperature to be of the order of 2% or less. However, a careful finite size extrapolation for the Yukawa system remains to be performed but is beyond the scope of this initial investigation.

The total potential energy for a system of N particles interacting via the Yukawa potential $V_Y(r)$ is given by [18],

$$V = \sum_{i>j}\sum_{\mathbf{L}} V_Y(\mathbf{r}_{ij} + \mathbf{L}) \;+\; \frac{1}{2}\sum_{i}\sum_{\mathbf{L}\neq 0} V_Y(\mathbf{L})\;, \tag{10}$$

where $\mathbf{r}_{ij} = \mathbf{r}_i - \mathbf{r}_j$, and $\mathbf{L}$ is a lattice vector. Instead of representing long-range terms, $V_P(\mathbf{r}) = \sum_{\mathbf{L}} V_Y(\mathbf{r}+\mathbf{L})$, on a 3D table [16], we adopt the optimized Ewald technique [19] by Natoli and Ceperley [20] and express the potential as

a sum of one real-space image, $W(|\mathbf{r}|)$, and a number of Fourier components,

$$V_P(\mathbf{r}) \equiv \sum_{\mathbf{L}} V_Y(\mathbf{r}+\mathbf{L}) \approx W(|\mathbf{r}|) + \sum_{|\mathbf{k}|\leq k_c} y_{\mathbf{k}} e^{+i\mathbf{kr}}. \tag{11}$$

Following Natoli and Ceperley [20], we express W as a linear combination of fifth-order polynomials, $W(|\mathbf{r}|) = \sum_n a_n f_n(|\mathbf{r}|)$, which is known as a locally piecewise-quintic Hermite interpolant. The fit coefficients a_n and $y_{\mathbf{k}}$ can be derived by minimizing the χ^2 deviation,

$$\chi^2 = \frac{1}{\Omega}\int_{\Omega} d^3\mathbf{r} \left[V_P(\mathbf{r}) - \sum_n a_n f_n(|\mathbf{r}|) - \sum_{|\mathbf{k}|\leq k_c} y_{\mathbf{k}} e^{+i\mathbf{kr}} \right]^2 , \tag{12}$$

where $\Omega = L^3$ is the volume of the unit cell. For the Fourier coefficients this directly yields,

$$y_{\mathbf{k}} = v_{\mathbf{k}} - \sum_n a_n f_{n\mathbf{k}} , \qquad \text{with} \qquad v_{\mathbf{k}} = \frac{1}{\Omega}\int_{\Omega} d^3\mathbf{r} V_P(\mathbf{r}) e^{-i\mathbf{kr}} , \tag{13}$$

where $v_{\mathbf{k}}$ and $f_{n\mathbf{k}}$ are the corresponding Fourier transforms. Deviating from [20], we derive the coefficients a_n from the following set of linear equations, $m = \{1, \ldots, n\}$,

$$\left[v_m - \sum_{|\mathbf{k}|\leq k_c} v_{\mathbf{k}} f_{m\mathbf{k}} \right] = \sum_n a_n \left[f_{nm} - \sum_{|\mathbf{k}|\leq k_c} f_{n\mathbf{k}} f_{m\mathbf{k}} \right] . \tag{14}$$

v_m and f_{nm} are overlap integrals, $f_{nm} = \frac{1}{\Omega}\int_\Omega d^3\mathbf{r} f_n(\mathbf{r}) f_m(\mathbf{r})$, and

$$v_m = \frac{1}{\Omega}\int_{\Omega} d^3\mathbf{r}\; V_P(\mathbf{r})\, f_m(|\mathbf{r}|) = \frac{1}{\Omega}\sum_{\mathbf{L}}\int_{\Omega} d^3\mathbf{r}\; V_Y(\mathbf{r})\, f_m(|\mathbf{r}|) \tag{15}$$

$$= \frac{4\pi}{\Omega}\int dr\, r^2\, V_Y(r) f_m(r) \;+\; \sum_{\mathbf{L}\neq 0} \frac{2\pi}{\Omega L}\int dr\, r\, f_m(r) \int_{L-r}^{L+r} dq\, q\, V_Y(q) \; . \tag{16}$$

In the last expression, one must sum over a sufficiently large number of images until the interaction is completely screened, $|\mathbf{L}| \gg D_s$. Computing the coefficients a_n using the real-space integration in Eq. 16 is more efficient and accurate than the Fourier integration employed in [20]. Our approach also works well for the Coulomb problem, which was the motivation for the [20] work. In this case, the Ewald potential replaces V_P in Eq. 12.

This optimized Ewald approach provides us with an accurate representation of the periodic functions leading to efficient many-body simulations. We apply it to the Yukawa potential, V_Y, to the corresponding pair action, U_Y, and also to the kinetic energy term, $\left(\frac{dU_Y}{d\beta} - V_Y\right)$, unless it is very small for $r \geq L/2$. Typically, we use between 10 and 20 shells of k vectors.

3 Results

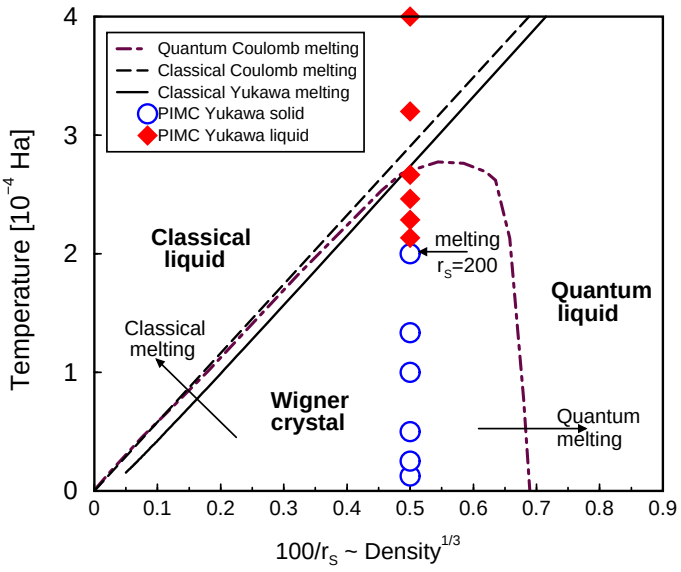

Fig. 2. Phase diagram for Wigner crystal. The dashed lines show the classical melting line, $\Gamma = 172$, and quantum melting line for Coulomb systems, computed by Jones and Ceperley [5] with PIMC. The solid lines show the classical melting line for the Yukawa system with the screening length chosen for hydrogen. Our PIMC simulations at $r_s = 200$ ($\circ$ and $\diamond$) show a significant reduction in the melting temperature below the classical value due to the quantum effects of the protons.

The phase diagram in Fig. 2 relates our simulations at a fixed density of $r_s = 200$ to the classical Yukawa melting computed by Hamaguchi, the classical Coulomb melting line given by $\Gamma = \frac{\mathbf{e^2}}{r_s k_b T} = 172$, and the quantum melting for Coulomb systems [5].

The most straightforward way to detect melting in the simulation is to monitor the instantaneous value of the Lindemann ratio, $\gamma = \sqrt{\langle u^2 \rangle}/r_{NN}$, which relates the average displacement of a particle from its original lattice site to the nearest neighbor distance. Fig. 3 shows the Lindemann ratio for three Monte Carlo simulations. At the beginning of each simulation, the particles are in the classical b.c.c. ground state. For temperatures sufficiently above the melting line, the system melts instantly. For temperatures only slightly above the melting line, the simulation shows a meta-stable superheated solid, which

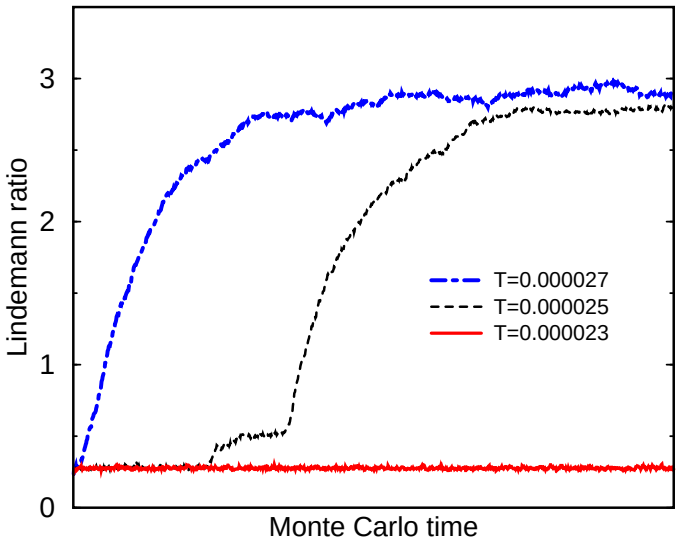

Fig. 3. The evolution of the Lindemann ratio is shown for the three Monte Carlo simulations in the vicinity of the melting temperature.

might melt at some point during the MC simulation, as the black dashed line indicates. The time it takes to melt depends not only on temperature, but also on system size, the type of MC moves, and the MC random numbers, thereby making this criterion impractical for determining the melting temperature.

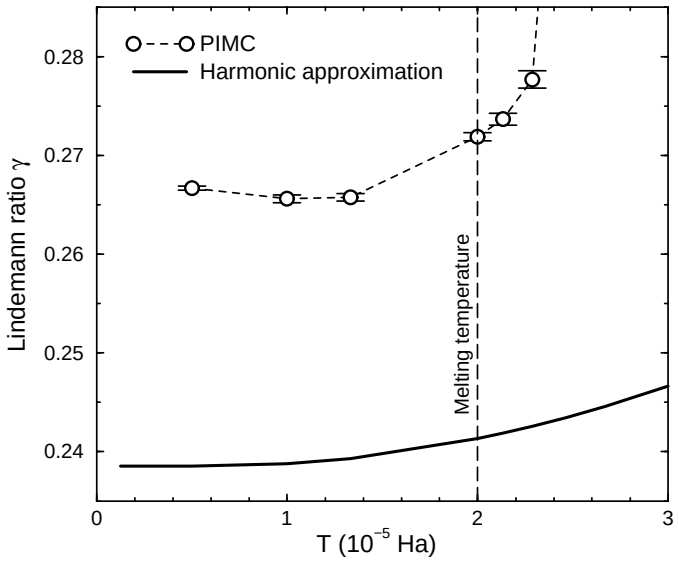

Fig. 4. The average Lindemann ratio derived from PIMC and from the harmonic lattice approximation.

The average values of the Lindemann ratio are shown in Fig. 4 as a function temperature. At the thermodynamic melting temperature of 2.0×10^{-5}, derived from free energy calculations to be discussed later, the Lindemann ratio has a value of 0.272. This number is not universal and its dependence on density and the interaction potential remains to be studied further.

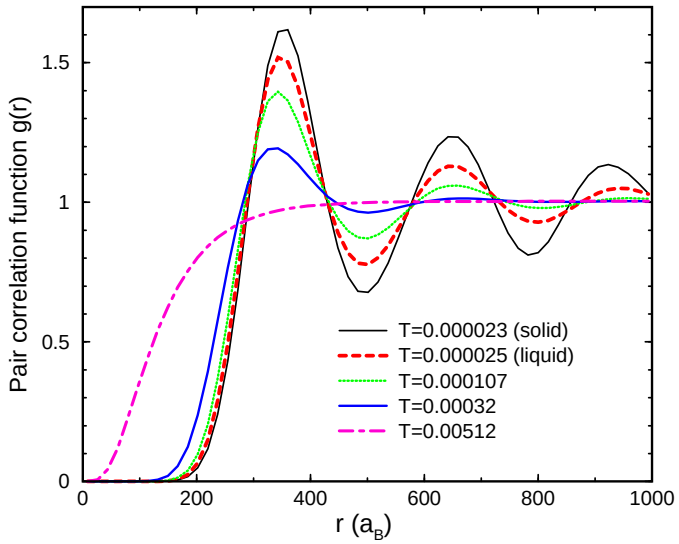

Fig. 5. Pair correlation functions, $g(r)$, for different temperatures.

Fig. 5 shows a series of pair correlation functions, $g(r)$, for simulations at different temperatures. The magnitude of the oscillations in the $g(r)$ show a significant temperature dependence in the liquid phase. However, there is only a small change upon melting, and all $g(r)$ functions in the solid phase are practically identical to the example shown for T=2.3×10^{-5}.

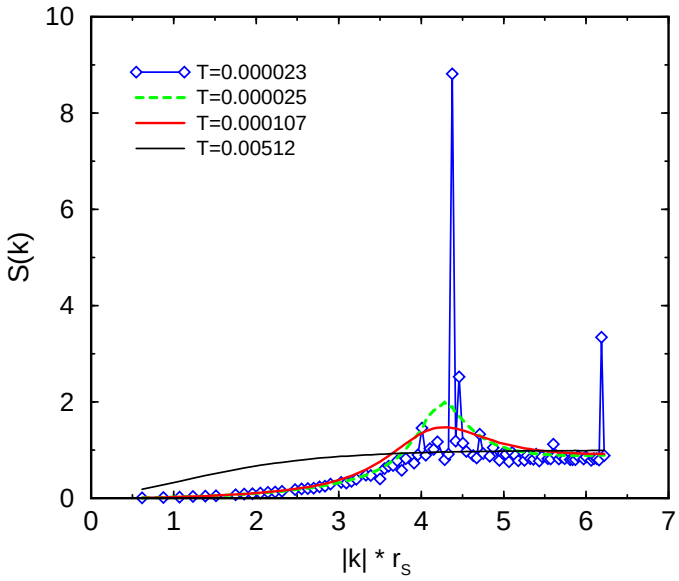

Fig. 6. The sharp peaks in the structure factor, $S(k)$, disappear when the system melts and a pattern typical for a liquid appears. This transition coincides with the increase in the Lindemann ratio.

Compared to the pair correlation function, the structure factor, $S(k)$, shows significant changes upon melting (Fig. 6). The disappearance of the peaks coincides with the increase in the Lindemann ratio beyond its stability limit of approximately 0.28. However, neither method can determine whether a

simulation is in the meta-stable state. They only lead to an upper bound of the melting temperature. To determine the thermodynamic phase boundary, one needs the free energy in both phases, which can be obtained through thermodynamic integration of the internal energies.

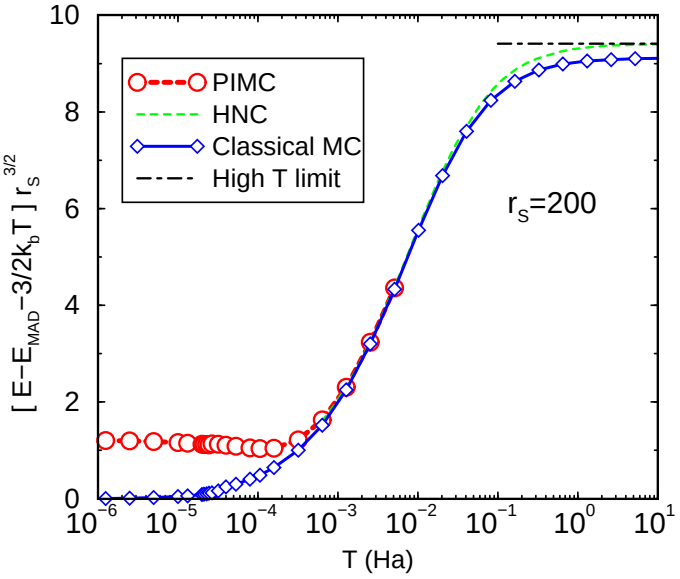

Fig. 7. The internal energy per particle is shown as a function of temperature. The classical kinetic energy and the Madelung term have been removed.

Fig. 7 compares PIMC internal energies with results from corresponding classical MC that we have performed. At high temperature when the thermal de Broglie wavelength is short compared to the inter-particle spacing, the protons behave classically and the PIMC energies approach results from classical MC simulations. At low T, both results differ substantially, due to the zero point motion. The simulation results do not exactly reproduce the analytical high T limit [16]. This discrepancy is caused by finite size effects, which become larger in the limit of high temperature where correlations are weak, and the Debye sphere increases as $T^{1/2}$. Therefore it eventually exceeds the size of any simulation cell. That is why we complemented our study with results from hyper-netted chain (HNC) calculations. Starting from the correct high temperature limit, the HNC results converge to the classical MC results at $\Gamma \approx 0.1$.

In Fig. 8, we compare MC results with our results derived from the harmonic lattice approximation and with the particle-in-a-cell (PIC) model. In the PIC approximation, one assumes that the thermal motion of the particles are uncorrelated. One freezes all particles in the supercell except one and derives all thermodynamic variables from the motion of this single classical particle. The PIC internal energies agree remarkably well with the corresponding classical MC results for the b.c.c. solid. However, a generalization of the PIC model to the quantum case is not straightforward. If one naively considers a quantum

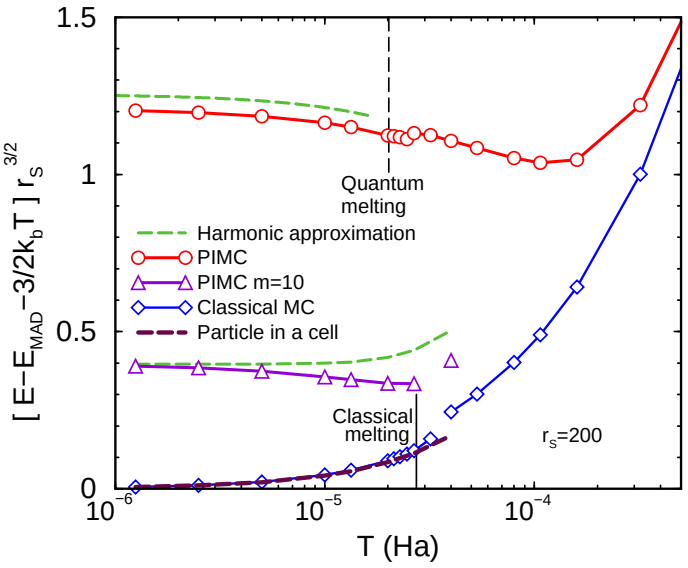

Fig. 8. Low temperature region of Fig. 7. Results from the harmonic lattice approximation and from a classical particle-in-a-cell model have been added. Furthermore, PIMC and harmonic results for particles with mass=10 instead of 1 have been included to demonstrate that the harmonic approximation becomes more accurate as zero point fluctuations are reduced.

particle represented by a path in a lattice of frozen classical particles, then the resulting kinetic energies are far too high (worse than the harmonic approximation), because the surrounding classical particles provide too high of a confining force due to the missing quantum fluctuations.

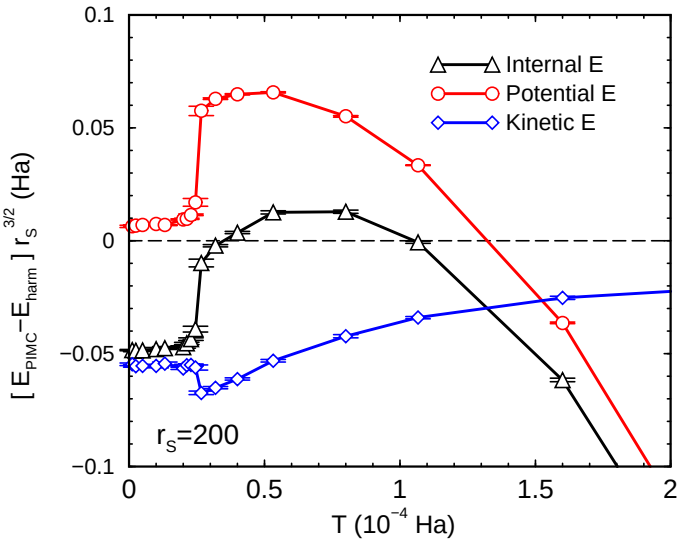

Fig. 9. Difference in internal, kinetic, and potential energy between PIMC and the harmonic lattice approximation. The sharp kinks near T=2.5×10^{-5} indicate the melting transition.

Fig. 8 also shows results from the harmonic lattice approximation for a unit

cell of corresponding size. Harmonic internal energies are significantly overestimated, primarily due to errors in the kinetic energy as demonstrated in Fig. 9. The zero point motion of the protons is large enough so that paths travel into regions of the potential where the harmonic approximation is no longer valid. The comparison of the PIMC Lindemann ratios and the corresponding harmonic values in Fig. 4 shows that the harmonic approximation localizes the particles too much, thereby increasing the kinetic energy. To further support this conclusion, we perform PIMC and harmonic calculation with particles 10 times as heavy. Fig. 8 shows that the agreement improves substantially.

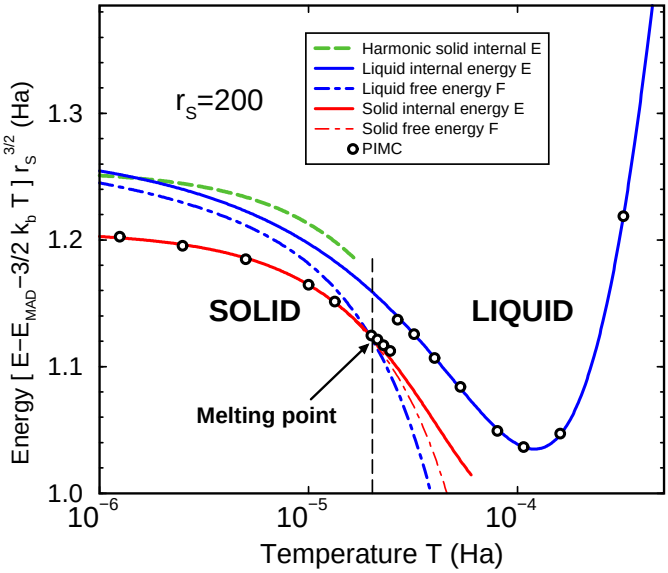

Fig. 10. Internal and free energies, E and F, are shown for the solid and liquid phase.

Fig. 10 shows the internal PIMC energies along with the free energies obtained from thermodynamic integration. The solid free energies agree very well with solid internal energies until melting, which suggest that each phonon mode is in its ground state. Excitations in the phonon spectra at higher temperature then directly lead to the melting of the crystal.

At low T, the free energies of the crystalline state are lower than the extrapolated values for the liquid, which means the solid phase is stable and the density of $r_s = 200$ is not yet high enough to reach the quantum melting transition at zero temperature (see Fig. 2).

At T=2.0×10^{-5}, the computed free energies of both phases match, which determines the thermodynamic melting point for the density of $r_s = 200$. For hydrogen, this corresponds to a temperature of 11,700 K, a mass density of 2,100 g cm^{-3}, and a pressure of approximately 3×10^{17} Pa.

This pressure result is dominated by the kinetic energy of the non-interacting

Fermi gas of electrons. At this high density of $r_s = 0.1$ in conventional atomic units, the Hartree-Fock Coulomb interaction of the electrons contributes only -2%, the Thomas-Fermi electron-proton interaction -0.4%, and the electron correlation in the homogeneous electron gas -0.02% to the total pressure.

Fig. 10 also shows that a number of simulations of the b.c.c. solid that appeared to be stable were actually meta-stable thermodynamically, since free energy calculations resulted into a lower melting temperature. This discrepancy was also observed in the classical simulation results shown in Fig. 8.

The melting temperature of 2.0×10^{-5} for the quantum system is significantly below the corresponding classical value of 2.7×10^{-5}, which demonstrates the importance of quantum effects. Furthermore, our Yukawa melting results suggest that the departure from the classical melting line occurs at lower densities and temperatures than predicted for Coulomb system by Jones and Ceperley [5].

4 Conclusions

In this article, we used many-body computer simulations of protons interacting via a Yukawa potential to model dense atomic hydrogen in the regime of the Wigner crystal. Path integral Monte Carlo simulations were employed to capture the quantum effects of the protons. Electronic screening effects were treated in the Thomas-Fermi approximation, which distinguishes our results from the earlier work by Jones and Ceperley [5].

We use the Lindemann ratio, pair correlation functions, and the structure factor to study the stability of the Wigner crystal and to detect melting. We observed that the system can remain in a meta-stable state of a super-heated crystal during the entire course of a PIMC simulation, which makes a direct determination of the melting temperature very difficult.

Instead, a reliable melting temperature can be obtained by matching of the free energies of both phases, which were derived by thermodynamic integration of the PIMC internal energies. For the density under consideration, $r_s = 200$, we found that the quantum Yukawa systems melts at significantly lower temperatures than the corresponding classical system.

Furthermore, we compared our PIMC results with other more approximate techniques. The harmonic lattice approximation overestimates the kinetic energies significantly because the zero point motion of the protons is strong enough so that anharmonic effects in the crystal field become relevant. We also compared with a classical particle-in-a-cell model and found good agreement

with classical MC simulation. However this method cannot be generalized easily to the case of quantum protons.

We plan to extend our analysis to other densities and to derive a phase diagram that indicates the stability of the Wigner crystal of nuclei in the presence of electronic screening effects. A careful analysis of finite size effects also remains to be done. Future theoretical work on dense atomic hydrogen will need to describe the electronic properties on a more fundamental level. Coupled ion-electron Monte Carlo is one promising approach [21].

5 Acknowledgments

We would like to acknowledge stimulating discussions with J. Kohanoff and M. Magnitskaya and thank J. Vorberger for providing us with HNC internal energies. This material is based upon work supported by NASA under the grant PGG04-0000-0116 and by the National Science Foundation under the grant No. 0507321. We acknowledge using computers at the National Center for Supercomputing Applications. R.L.G. received support from the National Science Foundation's Research Experiences for Undergraduates program at the Carnegie Institution of Washington.

References

[1] E. Gregoryanz, A. F. Goncharov, K. Matsuishi, H. Mao, and R. J. Hemley. *Phys. Rev. Lett.*, 90:175701, 2003.

[2] F. Datchi, P. Loubeyre, and R. LeToullec. *Phys. Rev. B*, 61:6535, 2000.

[3] T. Ogitsu, E. Schwegler, F. Gygi, and G. Galli. *Phys. Rev. Lett.*, 91:175502, 2003.

[4] S.A. Bonev, E. Schwegler, T. Ogitsu, and G. Galli. *Nature*, 431:669, 2004.

[5] M. D. Jones and D. M. Ceperley. *Phys. Rev. Lett.*, 76:4572, 1996.

[6] B. Militzer and D. M. Ceperley. *Phys. Rev. Lett.*, 85:1890, 2000.

[7] N. W. Ashcroft and N. D. Mermin. *Solid State Physics*. Harcourt, Inc., Orlando, FL, 1976.

[8] D. Ceperley, G. V. Chester, and M. H. Kalos. *Phys. Rev. B*, 16:3081, 1977.

[9] D. Ceperley and G. V. Chester. *Phys. Rev. B*, 17:1070, 1978.

[10] K. K. Mon, G. V. Chester, and N. W. Ashcroft. *Phys. Rev. B*, 21:2641, 1980.

[11] R. P. Feynman. *Phys. Rev.*, 90:1116, 1953.

[12] E. L. Pollock. *Comp. Phys. Comm.*, 52 :49, 1988.

[13] R. G. Storer. *J. Math. Phys.*, 9:964, 1968.

[14] B. Militzer and E. L. Pollock. *Phys. Rev. B*, 71:134303, 2005.

[15] D. M. Ceperley. *Rev. Mod. Phys.*, 67:279, 1995.

[16] S. Hamaguchi, R. T. Farouki, and D. H. E. Dubin. *Phys. Rev. E*, 56:4671, 1997.

[17] M.D. Jones and D.M. Ceperley. *Phys. Rev. Lett.*, 76:4572, 1996.

[18] M.P. Allen and D.J. Tildesley. *Computer Simulation of Liquids*. Oxford University Press, New York, 1987.

[19] P.P. Ewald. *Ann. Phys.*, 54:557, 1917.

[20] V. Natoli and D. M. Ceperley. *J. Comp. Phys.*, 117:171–178, 1995.

[21] C. Pierleoni, D. M. Ceperley, and M. Holzmann. *Phys. Rev. Lett.*, 93:146402, 2004.